



HAL
open science

CO₂ methanation over LDH derived NiMgAl and NiMgAlFe oxides: Improving activity at lower temperatures via an ultrasound-assisted preparation

Michel Obeid, Christophe Poupin, Madona Labaki, Samer Aouad, Sharad Gupta, Haingomalala Lucette Tidahy, Aida Younis, Ferdaous Ben Romdhane, Eric Gaigneaux, Josefine Schnee, et al.

► To cite this version:

Michel Obeid, Christophe Poupin, Madona Labaki, Samer Aouad, Sharad Gupta, et al.. CO₂ methanation over LDH derived NiMgAl and NiMgAlFe oxides: Improving activity at lower temperatures via an ultrasound-assisted preparation. Chemical Engineering Journal, 2023, 474, pp.145460. 10.1016/j.cej.2023.145460 . hal-04212860

HAL Id: hal-04212860

<https://hal.science/hal-04212860>

Submitted on 20 Sep 2023

HAL is a multi-disciplinary open access archive for the deposit and dissemination of scientific research documents, whether they are published or not. The documents may come from teaching and research institutions in France or abroad, or from public or private research centers.

L'archive ouverte pluridisciplinaire **HAL**, est destinée au dépôt et à la diffusion de documents scientifiques de niveau recherche, publiés ou non, émanant des établissements d'enseignement et de recherche français ou étrangers, des laboratoires publics ou privés.

CO₂ methanation over LDH derived NiMgAl and NiMgAlFe oxides: Improving activity at lower temperatures via an ultrasound-assisted preparation

Michel OBEID^{a,b}, Christophe POUPIN^{*a}, Madona LABAKI^b, Samer AOUAD^c, François DELATTRE^a, Sharad GUPTA^a, Haingomalala Lucette TIDAHY^a, Aida YOUNIS^c, Ferdaous BEN ROMDHANE^d, Eric M. GAIGNEAUX^e, Josefine SCHNEE^f and Edmond ABI-AAD^a

a Unité de Chimie Environnementale et Interactions sur le Vivant, UR 4492, Univ. Littoral Côte d'Opale, 145 avenue Maurice Schumann 59140, Dunkerque, France

*E-mail: Christophe.poupin@univ-littoral.fr

b Laboratory of Physical Chemistry of Materials (LCPM/PR2N), Lebanese University, Fanar, P.O. Box 90656, Jdeidet El Metn, Lebanon

c Department of Chemistry Faculty of Arts and Sciences, University of Balamand, Kelhat, Deir El Balamand, Lebanon

d Fédération de Chimie et Matériaux de Paris-Centre (FCMat), Campus Pierre et Marie Curie, 4 Place Jussieu, F-75005 Paris Cedex 05, France

e Institute of Condensed Matter and Nanosciences (IMCN), Molecular Chemistry, Materials and Catalysis (MOST), Université catholique de Louvain, Pl. Louis Pasteur 1, L4.01.09, 1348 Ottignies-Louvain-la-Neuve, Belgium

f Laboratoire de Réactivité de Surface (LRS), CNRS, Sorbonne Université, Campus Pierre et Marie Curie, 4 Place Jussieu, F-75005 Paris Cedex 05, France

Abstract: Within the idea to catalyze CO₂ methanation NiMgAl and NiMgAlFe oxides were synthesized by the layered double hydroxide route using co-precipitation and ultrasound-assisted co-precipitation. MgAl and MgAlFe oxides-supported Ni materials prepared by the impregnation method were used as references. Inductively-coupled plasma optical emission spectroscopy, X-ray diffraction, thermal decomposition, H₂-temperature programmed reduction, N₂ physisorption, and transmission electron microscopy were used to characterize the catalysts. NiMgAl prepared using ultrasound-assisted co-precipitation showed the best activity with no deactivation for 40 h under stream. This was attributed mainly to the lower particle size, the higher specific surface area and pore volume as well as the better dispersion of nickel active species at the surface of the concerned materials. In our case, the ultrasound method saves a lot of time during the synthesis process since the maturation phase lasts only 30 min instead of 18 h required for the traditional co-precipitation.

Keywords: Layered double hydroxide • Nickel • Methanation • Ultrasound • CO₂ hydrogenation

2 Global climate change and the gradual depletion of fossil fuels are two of the most pressing issues
3 confronting humanity today [1]. The usage of renewable energy sources (RES), like wind or
4 photovoltaics, is one of the developed solutions [2]. However, they are intermittent [3]. The demand for
5 power from end-users differs with the generation of electricity from RES, implying a potential electrical
6 network imbalance. Power-to-Gas (PtG) is a potential long-term and high-capacity renewable energy
7 storage option. This concept can be an interesting way to use excess electricity to produce H₂ from water
8 electrolysis. However, safety concerns like a wide flammability interval, as well as storage and
9 transportation constraints (e.g., poor energy density, steel embrittlement) limit hydrogen's direct usage
10 [4]. Hydrogen can react with CO₂ stored or emitted according to the Sabatier reaction (Eq. 1).



12 This reaction enables the production of synthetic natural gas (SNG) methane that has a very high-energy
13 value, can be injected into the natural gas network, and can be directly used as a fuel in the transportation
14 sector [5]. The CH₄ produced offers a potential solution in order to manage fluctuating output of
15 renewable energy and mitigate CO₂ emissions at the same time [6]. However, even though the CO₂
16 methanation reaction is thermodynamically possible in a practical range of conditions, it remains
17 kinetically limited [7]. An efficient catalyst will increase the rate of the methanation reaction, exhibit high
18 activity, selectivity and stability within an appropriate temperature range, while taking into account
19 economic constraints [8]. Several metals in the periodic table's group VIII, including Ni, Co, Fe, Ru, and
20 Rh, are capable of undergoing the methanation process [9–11]. The Earth-abundant Ni-based catalysts
21 have long been the top option for industrial applications [12,13]. Furthermore, many oxides have been
22 studied as potential supports for the methanation reaction such as: CeO₂, TiO₂, MgO, Sm₂O₃, CeO₂/ZrO₂,
23 etc [13,14]. The stabilization of the active metal on these supports is very crucial to achieve good catalytic
24 activity and stability. However, the exothermic nature of the methanation reaction, results in the thermal
25 aggregation of metallic Ni active sites by hotspots formation in the catalytic bed. As a consequence, the
26 catalysts become less stable. In order to solve these issues, improved properties and well-defined
27 crystalline structures of supports frequently stabilize Ni active sites [15].

28 In this context, layered double hydroxide structures (LDH) gained a lot of interest as CO₂ methanation
29 catalyst precursors [16]. Indeed, they allow getting catalysts with well crystalline structure, high specific
30 surface area, small metal particle sizes, good thermal stability, and uniform distribution of active sites
31 [17].

32 The LDH has the general formula: [(M²⁺)_{1-x}(M³⁺)_x(OH)₂](Aⁿ⁻)_{x/n}·mH₂O, where M is a metal and A is an
33 anion. The divalent cations M²⁺ can be Mg²⁺ and/or another one, while the trivalent cation M³⁺ can be
34 Al³⁺ and/or something else [18]. Different possibilities are offered for the anions. Since a wide choice of
35 cations and anions is possible, LDH-type materials are promising candidates in heterogeneous catalysis.

36 Therefore, oxides deriving from LDH are often used as active phase supports or as catalysts [19].
37 Different preparation methods such as co-precipitation, urea hydrolysis and sol-gel methods can be used
38 for the synthesis of the LDH structure [20–22]. Co-precipitation is the most common and generally used
39 process [23]. In order to obtain well-nanocrystallized materials, co-precipitation has been coupled to
40 ultrasound treatment [24]. In addition, the use of ultrasound during the synthesis of catalytic materials
41 showed many advantages over traditional approaches [24]. In this process, acoustic cavitation bubbles
42 collapse into each other, generating high temperatures and pressures developing hot spots [25], resulting
43 in solids with small homogeneous particles and increased specific surface area [26]. Enhanced catalytic
44 activity, selectivity, and stability are all a result of these features [27]. The preparation of LDH using
45 ultrasound routes have received a lot of interest recently due to their efficiency, affordability, simplicity,
46 large specific surface area, adjustable and well-dispersed particle sizes [28–30]. In the present work,
47 nickel was chosen as an active phase due to its high activity and relatively low cost [31]. It can be
48 introduced into the catalysts directly by substituting partially the magnesium or can be added by
49 impregnation the mixed oxides obtained after the treatment of LDH. Magnesium was used to increase the
50 basicity. Its interaction with the nickel phase is known to lead to its better distribution allowing the
51 capture of CO₂ [32]. In addition, MgO issued from LDH plays an important role as an active site for the
52 activation of CO₂ to form carbonate/hydrocarbonate species that react with hydrogen to form methane
53 [33], while the presence of aluminum ensures a high specific surface area [34,35]. According to the
54 literature, the partial substitution of Al by small quantities of iron is performed to improve the reducibility
55 of nickel species [36]. Thus, to explore the potential of having a high quantity of iron on the reducibility
56 of the catalyst and on the catalytic activity, we chose the composition of 14wt% of iron.

57 The objective of this work is the examination and comparison of the catalytic properties in the CO₂
58 methanation reaction of (NiMgAl, NiMgAlFe) prepared by three different routes (traditional co-
59 precipitation (Cp), ultrasound-assisted co-precipitation (US), and impregnation method (Imp)). The
60 originality of this work is the differentiation of the three above-mentioned preparation methods for the
61 chosen material, a question that has not been addressed before in the context of CO₂ methanation.
62 Furthermore, the US method can be used in different ways (during co-precipitation and in the maturation
63 phase). Contrary to other works, the present paper explores in a rigorous way the operating conditions
64 used in the US method such as ultrasonic power, frequency, time and mode, which can indeed have a
65 significant impact on the synthesis results and consequently on the catalytic performances and allow the
66 comparison of the obtained results with the future studies. These operating conditions are then explained
67 in the experimental section. We also investigated the effect of a high quantity of iron on the catalytic
68 performance.

69 **2. Materials and methods**

70 **2.1. Catalysts preparation**

71 Co-precipitation, ultrasound-assisted co-precipitation, and wet impregnation were used to synthesize our
72 catalysts.

73 First, NiMgAl, NiMgAlFe, MgAl, and MgAlFe layered double hydroxides based on Ni (II), Mg (II), Al
74 (III), and Fe(III) were prepared by co-precipitation thoroughly described in previous studies [37]. The
75 solution containing the desired metal salts is added dropwise to deionized water with the Na₂CO₃ (1
76 mol.L⁻¹) solution, whose pH is adjusted to 9 by a basic NaOH (2 mol.L⁻¹) solution. After precipitation, the
77 resulting mixture was stirred for 18 hours (maturation step). Then, the mixture was filtered and the
78 precipitate was washed with hot deionized water until a neutral pH was obtained. This washing allows the
79 removal of soluble ions (nitrate, Na⁺,...). After having been placed 48 h in the oven at 60 °C, the solid
80 obtained was manually ground to powder in an agate mortar. It should be noted that in our preparations,
81 we took a molar ratio M(II)/M(III) = 3. In all cases, Ni content was 10wt%. When substituting Al³⁺ by
82 Fe³⁺, the molar ratio Al/Fe is equal to 1.

83 Second, regarding the ultrasound-assisted co-precipitation method, the same preparation steps were used,
84 but in the maturation phase instead of lasting for 18 h under agitation, ultrasound irradiations (50 W,
85 pulse mode of 30s on, 30s off) were used for 30 minutes and were carried out on a device driven by a
86 Nextgen frequency generator (SinapTec ultrasonic technology). The apparatus used in this maturation
87 step consists in an ultrasonic pipe with a volume of 700 ml. It is equipped with eight ultrasonic
88 transducers at 22 kHz with a maximum output power of 400 W.

89 Third, the wet impregnation method is used to synthesize impregnated catalysts that serve as reference
90 materials. In the same purpose, Ni was impregnated on the mixed oxides derived from MgAl or MgAlFe
91 LDH prepared by the co-precipitation method. In order to obtain the desired materials, all samples were
92 calcined under air at 800 °C and reduced under pure hydrogen at 800 °C. For better comprehension, the
93 synthesis protocols for each of the samples are summarized in table S1 in the supplementary information
94 sheet.

95 **2.2. Catalysts characterization**

96 The XRD analyses were performed on a BRÜKER D8 diffractometer at room temperature. All samples'
97 scattering intensities were measured with a step size of 0.02 ° for an integration of 2 s throughout an
98 angular range of 5 ° < 2θ < 80 °. Phase identification was accomplished by comparing the diffraction
99 patterns to the common XRD reference patterns in the JCPDS database.

100 Differential thermal or thermogravimetric analysis (DTA/TG) was carried out on a NETZSCH STA 409
101 starting from ambient temperature up to 1000 °C (temperature rise of 5 °C.min⁻¹) under an airflow of
102 100 mL.min⁻¹. For each analysis, the weight of the test sample was about 10 mg. The software "Universal
103 analysis" is used to process the results obtained.

104 The actual Ni, Mg, Al and Fe weight contents of the prepared materials were assessed by inductively-
105 coupled plasma optical emission spectroscopy (ICP-OES) with an Agilent 5100 SVDV spectrometer.
106 Samples were mineralized typically as follows. 50 mg of powder was digested with 1 mL of HNO₃ (65%
107 Normatom) at 80-90 °C during 4-6 h and then diluted in 50 mL of ultrapure water. 1 mL of the latter
108 solution was finally diluted by adding HNO₃(2%) until obtaining a total volume of 10 mL. For each
109 analysis, three replicates were performed. Blanks were also analyzed to monitor instrument and digestion
110 procedure contamination. Standard solutions were prepared from pluri-elemental and mono-elemental
111 standards (SCP Science) and analyzed for calibration and quality control (drift, reproducibility, and
112 accuracy). The concentration of each element was calculated as the average of the data recorded with 3 or
113 4 wavelengths.

114 Temperature programmed reduction (H₂-TPR) experiments were carried out in a Micromeritics
115 Autochem II chemisorption analyzer. About 50 mg of sample were deposited in a quartz tube and
116 pretreated under an argon flow of high purity. This argon flow of 50 mL.min⁻¹, circulates under a
117 temperature ranging from ambient to 150 °C with a rise of 5 °C.min⁻¹ under Ar flow. This pretreatment is
118 done to eliminate atmospheric contaminants and water molecules. After this pretreatment, the sample was
119 cooled to room temperature under Ar flow, and then the catalyst is heated to 900 °C with a rise of
120 5 °C.min⁻¹ under a H₂ flow (5 % H₂ in Ar, 50 mL.min⁻¹) followed by naturally cooling down under an Ar
121 flow.

122 Textural analysis was performed on a Micromeritics 3Flex version 5.03 instrument. The pre-treatment is
123 done under vacuum (continuous draft) at 350 °C for 4 h. The tubes are weighed and then a N₂
124 physisorption analysis is performed. When the analysis started, the tubes are dipped in a liquid nitrogen
125 bath at -196 °C. The specific surface is determined by the Brunauer-Emmett-Teller (BET) method. The
126 Barrett-Joyner-Halenda (BJH) method was used to determine pore distribution and pore volume.

127 Transmission Electron Microscopy (TEM) analyses were carried out using a JEOL 2100Plus UHR
128 microscope operating at 200kV. The powdered materials were dispersed in ethanol, and then, a drop was
129 evaporated on a carbon-coated copper grid. Mean surface diameters ($d=(nidi3)/(nidi2)$) were calculated
130 by measuring at least 300 particles for each examined sample from TEM images. Scanning transmission
131 electron microscopy (STEM) images using a high-angle annular dark-field (HAADF) detector were

132 acquired. The image contrast in this mode is strongly correlated with the atomic number: heavier elements
133 contribute to brighter contrast (Z-contrast). Analytic investigations were performed with an energy
134 dispersive X-ray spectrometer (EDX) attached to the microscope column.

135 2.3. Catalytic tests

136 The catalytic activity was examined at atmospheric pressure, in a fixed-bed U-shape reactor with a K-type
137 thermocouple at temperatures ranging from 100 °C to 400 °C. 150 mg of catalyst diluted with SiC to
138 achieve a catalytic bed volume of 1 cm³ was placed in the reactor. Before the test, the catalysts are
139 reduced for 2 hours at 800 °C (5 °C/min) under pure hydrogen flow of 20 mL/min. After cooling, the
140 reactor is fed with a gas mixture of CO₂/H₂/N₂ with respective volume ratios 10/40/50 with a total flow
141 rate of 100 mL/min (GHSV=6000h⁻¹). The reaction temperature is increased from 100 to 400 °C with a
142 rise of 5 °C/min. Each temperature step is maintained for 30 min. A gas chromatography system from
143 Global Analyser Solutions is used to analyze the reagents (CO₂ and H₂) as well as the reaction products
144 (CH₄ and CO). There are two analytical modules in it. The CO₂ gas is separated using the RTQ bond
145 module, while the H₂, CO, and CH₄ gases are separated using the Molsieve 4A module. These compounds
146 are detected using thermal conductivity detectors (TCD₁ and TCD₂). The quantification of the reagents
147 (CO₂ and H₂) and products (CO and CH₄) present in the reaction was done from the values obtained from
148 the chromatograms and the calibrations carried out for each gas. The general formulas used for the
149 calculations of conversions and selectivities are given below (Eq. 2, 3, and 4)

150

151 • Conversion of CO₂: $X_{CO_2} (\%) = \frac{n_{CO_2 \text{ in}} - n_{CO_2 \text{ out}}}{n_{CO_2 \text{ in}}} \times 100$ (Eq. 2)

152

153 • Selectivity of methane: $S_{CH_4} (\%) = \frac{n_{CH_4 \text{ formed}}}{n_{CO_2 \text{ in}} - n_{CO_2 \text{ out}}} \times 100$ (Eq. 3)

154

155

156 • Selectivity of CO: $S_{CO} (\%) = \frac{n_{CO \text{ formed}}}{n_{CO_2 \text{ in}} - n_{CO_2 \text{ out}}} \times 100$ (Eq. 4)

157

158 nCO_{2in} and nCO_{2out} are respectively the number of moles of CO₂ at the inlet and the outlet of the reactor,

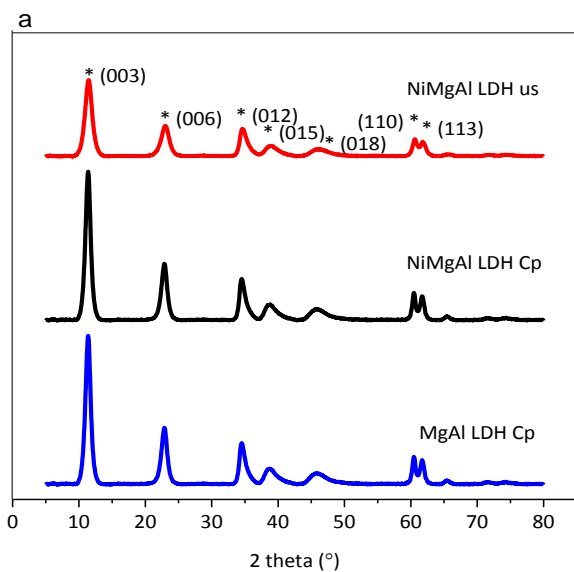
159 nCH_{4 formed} and nCO_{formed} are respectively the number of moles of CH₄ and CO obtained.

160 3. Results and Discussion

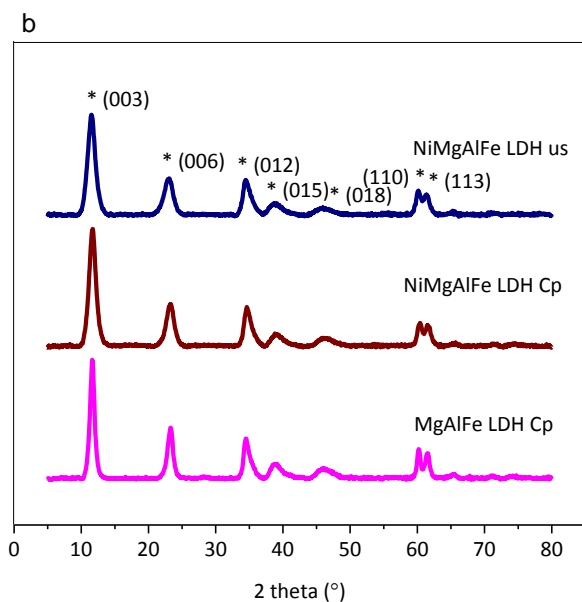
161 3.1. Characterization of the dried samples

162

163 The theoretical molar formulas are $\text{Ni}_{0.62}\text{Mg}_{5.38}\text{Al}_2$ LDH, $\text{Ni}_{0.62}\text{Mg}_{5.38}\text{AlFe}$ LDH for the samples prepared
164 by co-precipitation and ultrasound-assisted co-precipitation method for each series, and Mg_6Al_2 LDH,
165 Mg_6AlFe LDH for the support before impregnation. The X-ray diffractograms of the dried samples
166 (before calcination) are shown in Figure 1. The diffraction lines of LDH structure may be seen in the
167 patterns of all the prepared solids (JCPDS 22-0700).
168



169



170

171

172 **Figure 1.** X-ray diffraction patterns of the dried samples prepared by conventional co-precipitation (Cp)
 173 and by co-precipitation assisted by ultrasound (US). (a) MgAl and NiMgAl samples; (b) MgAlFe and
 174 NiMgAlFe samples. *: Layered double hydroxide phase (JCPDS N° 22-0700).

175 The diffraction peaks are observed at 2θ of 11.5 °, 23.5 °, 35.0 °, 38.0 °, 46.2 °, 60.5 °, and 61.8 ° and are
 176 respectively indexed to the lattice planes (003), (006), (012), (015), (018), (110), and (113) [38].
 177 Furthermore, aside from the typical LDH lines, no other lines were detected, showing that pure LDH was
 178 successfully synthesized in all the solids. Bragg's law, which is provided by the relation in the
 179 supplementary material sheet, is used to calculate the inter-planar spacing (d_{hkl}) that corresponds to these
 180 peaks. The different cell parameters are given in Table 1. Two parameters “a” and “c” should be
 181 evaluated for a LDH structure since it crystallizes in a 3R rhombohedral reticular system [38]. Knowing
 182 the lattice planes (hkl) and the inter-planar spacing (d_{hkl}), the cell parameters can be determined [24,39]
 183 The calculation details of the cell parameters are presented in the supplementary material sheet.

184 **Table 1.** Cell parameters (a and c) and crystallite size of the dried samples.

Dried solid		a (Å)	c (Å)	Crystallite size (Å) ^[a]
MgAl Cp	LDH	3.06	23.11	104
NiMgAl Cp	LDH	3.06	23.19	80
NiMgAl US	LDH	3.06	23.09	58
MgAlFe Cp	LDH	3.07	22.78	103
NiMgAlFe LDH Cp		3.06	23.11	68
NiMgAlFe LDH US		3.07	22.73	60

185 [a] Determined by Debye-sherrer equation.

186
 187 Table 1 lists the crystallographic parameters “a” and “c” of the dried solids determined by XRD
 188 measurements. As predicted, there is not any remarkable difference for the “a” parameter for both series
 189 of samples, since the crystallographic parameter “a” corresponds to the average cation-cation distance in a
 190 hydroxide sheet [39]. Indeed, the values of the radii of Fe³⁺ and Ni²⁺ cations do not differ much from that
 191 of Al³⁺ and Mg²⁺, respectively. Regarding the crystallographic parameter "c", which provides details on
 192 the interlayer domain's thickness [40], a decrease of this parameter is noticed when the ultrasound-
 193 assisted co-precipitation method is used. The electrostatic interactions between the sheets are thus
 194 strengthened leading to a more "compact" LDH structure as the ultrasound is used in the aging phase.
 195 These results are in agreement with Macedo et al. [41] who obtained a decrease in the values of the c
 196 parameter of NiMgAlCe LDH structure when using ultrasound during the aging phase. The intensity of

197 the indexed peaks decreases when using ultrasound in the aging phase (Figure 1). The crystallite size of
198 LDHs prepared by ultrasound-assisted co-precipitation is smaller compared to the sample prepared by
199 conventional co-precipitation (Table 1). This effect was also found by Climent et al. [42] who synthesized
200 a series of LDHs using ultrasound in the preparation method. This phenomenon is attributed to the
201 collapse of cavitation bubbles which causes a shock wave and micro-jets on the surface of the particles
202 leading to their breaking [43]. Moreover, the use of ultrasound in the solution results in generation of
203 sufficient nuclei, thereby lowering the supersaturation available for further growth [44]. Thus, ultrasound
204 can be used to control nucleation rates [45]. Furthermore, thermal decomposition analyses were
205 conducted over all the LDH samples. Three endothermic peaks are observed for all solids. Each peak
206 corresponds to a mass loss. The first peak, is due to the loss of physisorbed water from the outer surface
207 of the crystallites. The second peak and the third peak are due to the collapse of the LDH structure and the
208 formation of metal oxides [46]. These three weight loss zones are characteristic of LDH and therefore, in
209 this study, further confirms that LDH structure was achieved for all the samples via different preparation
210 methods. The DTA/TG profiles for all the samples are shown in Figure S2 in the supplementary material
211 sheet. Finally, it is worth mentioning that at 800 °C, the LDH structure is destroyed in all our samples.
212 Moreover, from this temperature, the recorded mass loss is negligible. Hence this temperature was chosen
213 for the treatment of the synthesized dried solids.

214

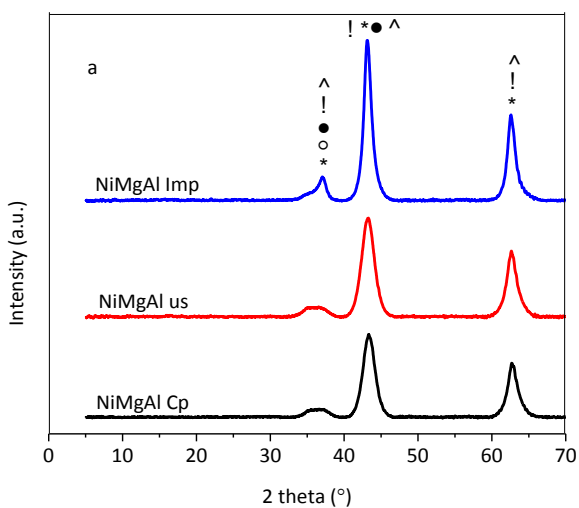
215 **3.2 Characterization of calcined samples**

216

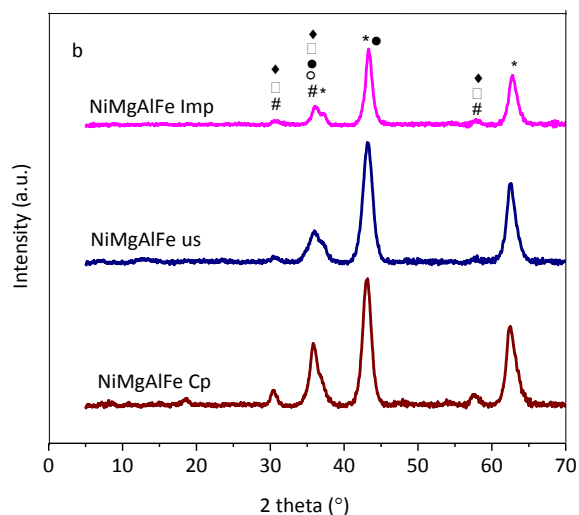
217 Figure 2 shows the X-ray diffractograms of NiMgAl and NiMgAlFe prepared by the three preparation
218 methods used and calcined at 800 °C. The diffractograms of all NiMgAl samples prepared by the three
219 preparation methods were compatible with the following structures: MgO periclase, cubic structure of
220 MgNiO₂ or rhombohedral structure of NiO, and spinel oxides NiAl₂O₄ and MgNiO₂. The X-ray
221 diffractograms for the NiMgAlFe samples show the presence of new phases corresponding to Fe₂O₃ [47],
222 Fe₃O₄ and NiFe₂O₄ [48] at $2\theta = 31^\circ$, 36° and 58° , respectively. Indeed, these samples with a molar ratio
223 $Al^{3+}/Fe^{3+} = 1$ possess a high iron weight content. As a result, the formation of iron oxides may be due to
224 the high iron content present in this solid [47]. Moreover, we note that the change in the preparation
225 method does not affect the formation of crystalline phases.

226

227



228



229

230 **Figure 2.** X-ray diffraction patterns of the calcined samples (a) the NiMgAl samples, (b) the NiMgAlFe,
 231 samples.

232 * MgO periclase JCPDS N° 43-1022, ! MgNiO₂ cubic JCPDS N° 24-0712, ^ NiO rhombohedral JCPDS

233 N° 44-1159, ● MgAl₂O₄ JCPDS N° 75-0713, # Fe₂O₃ Maghemite JCPDS N° 39-1346, ○ NiAl₂O₄ JCPDS

234 N° 65-3102, ◆ Fe₃O₄ Magnetite JCPDS N° 98-3854, □ NiFe₂O₄ Trevorite JCPDS N° 86-2267.

235 In heterogeneous catalysis, it is essential to understand the textural characteristics of the resulting oxides.

236 Some catalytic behaviors can be explained by the specific surface area, the pore diameter, the pore

237 volume and the pore type. These characteristics also give us information about the accessibility of the

238 active sites to the reagents. The nitrogen adsorption and desorption isotherms for all the samples are

239 shown in figure S3 in the supplementary material sheet. According to the IUPAC classification [49], all

our mixed oxides have a type IVa isotherm. Thus, the preparation method has no effect on the type of isotherms. On the other hand, we notice an effect on the type of hysteresis loop. More details concerning this issue are found in the supplementary material sheet. Table 2 shows the textural features and elemental composition of the prepared solids after calcination at 800 °C. The experimental metal loading are very close to the nominal contents in the catalysts with no big difference between the three methods of preparation. The specific surface area and pore volume increase when ultrasonic irradiation was applied during co-precipitation. Ultrasonic irradiation significantly alters the morphology of the particles on the surface. It creates small nanoparticles with a uniform dispersion which led to the increase of the available surface area [50]. However, these values decrease when the active phase (nickel) is added by impregnation, suggesting a clogging of the pores during the addition of the active phase. The specific surface area varies in the following order for the first series: NiMgAl US>NiMgAl Cp>NiMgAl Imp, similarly for the second series, it varies in the following order: NiMgAlFe US>NiMgAlFe Cp>NiMgAl Imp. Moreover, the specific surface area of the iron-containing samples is smaller than that of the iron-free samples regardless of the preparation method used. This may be due to the formation of Fe₂O₃ following the addition of iron. In fact, Fe₂O₃ has a very small specific surface area compared to Al₂O₃ [51]. Regarding the pore diameter, we obtained average diameters between 6 and 12 nm confirming that we obtained mesoporous materials. The use of ultrasound leads to an increase in pore volume, whereas the addition of the active phase by impregnation leads to a decrease in pore volume.

Table 2. Specific surface area, pore diameter, pore volume and experimental metal loading of the calcined samples

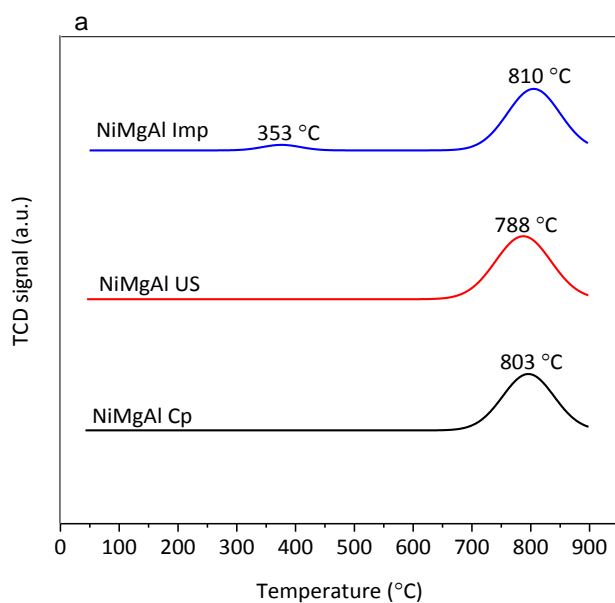
Catalyst	$S_{\text{BET}}^{[\text{a}]}$ ($\text{m}^2 \cdot \text{g}^{-1}$)	$D_p^{[\text{b}]}$ (nm)	$V_p^{[\text{b}]}$ ($\text{cm}^3 \cdot \text{g}^{-1}$)	$\text{Ni}^{[\text{c}]}$ (wt%)	$\text{Mg}^{[\text{c}]}$ (wt%)	$\text{Al}^{[\text{c}]}$ (wt%)	$\text{Fe}^{[\text{c}]}$ (Wt%)
NiMgAl Cp	202	9.8	0.44	9.01	28.75	12.91	-
NiMgAl US	232	11.1	0.74	9.28	29.58	13.56	-
NiMgAl Imp	162	6.7	0.38	9.36	30.59	13.01	-
NiMgAlFe Cp	125	12.8	0.46	10.42	24.6	7.39	16.37
NiMgAlFe US	139	13.4	0.55	7.947	25.63	5.81	12.54
NiMgAlFe Imp	120	6.7	0.31	8.705	31.43	7.02	15.29

[a] determined by BET method. [b] determined by BJH method. [c] determined from ICP-OES analysis.

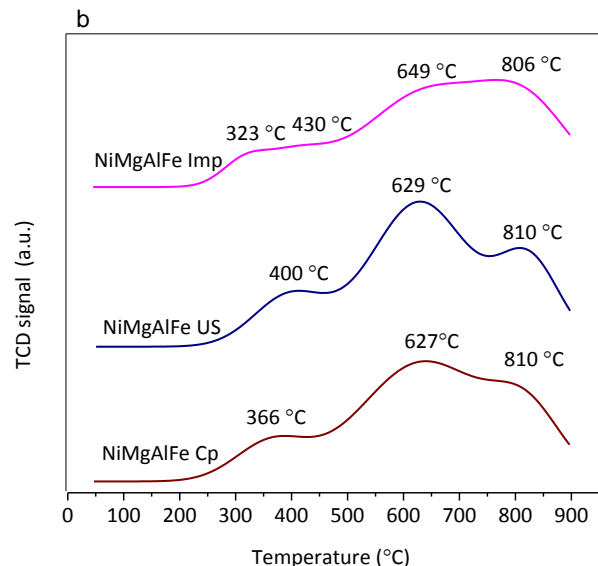
.

263 The H₂-TPR profiles of the different NiMgAl and NiMgAlFe solids are shown in Figure 3. It is to be
264 mentioned that aluminum and magnesium oxides are not reduced in our TPR conditions [52]. First of all,
265 for the samples NiMgAl in figure 3 (a), nickel oxide species are reduced at high temperatures (810, 788
266 and 803 °C, peak 2) as a result of spinel formation [53], which is suggested to occur by the XRD study.
267 For the sample NiMgAl Imp, we note a lower temperature reduction peak (353 °C, peak 1) attributable to
268 nickel oxide weakly interacting with the support [53]. Due to the production of spinel, a characteristic of
269 catalysts formed from hydrotalcite-like precursors, which was evoked in the XRD examination of the
270 calcined samples, the reduction temperatures of NiMgAl mixed oxides are high. This suggests that the
271 nickel ions in the solid matrix have strong interactions, which makes it difficult for NiO species to be
272 reduced at lower temperatures. This difficulty in the reduction of nickel species makes it more resistant
273 towards sintering, resulting in an ability to maintain high dispersion of Ni⁰ [48]. The experimental values
274 of H₂ consumptions (presented in table 3) are close to those obtained theoretically ($1.7 \times 10^3 \mu\text{mol.g}^{-1}$).
275 For the calculation of the theoretical amount of hydrogen, it was assumed that the nickel is in the form of
276 NiO and has been reduced into Ni⁰. The experimental value ($1.68 \times 10^3 \mu\text{mol.g}^{-1}$) of the amount of
277 hydrogen consumed for both samples NiMgAl Us and NiMgAl Imp are very close to the theoretical one
278 ($1.7 \times 10^3 \mu\text{mol.g}^{-1}$). This may be due to a better dispersion of the active phase rendering it more
279 accessible to the reducing agent. The lower experimental value of hydrogen consumption (1.33
280 $\times 10^3 \mu\text{mol.g}^{-1}$) of NiMgAl Cp indicates that part of the species has not been completely reduced into
281 metallic ones.

282
283



284



285

286 **Figure 3.** H₂-temperature programmed reduction (TPR) profiles. (a) NiMgAl samples, (b) NiMgAlFe
 287 samples.

288 Concerning the H₂-TPR of the iron-containing samples in figure 3 (b), we note the presence of three
 289 reduction peaks for the samples prepared by co-precipitation and ultrasonically assisted co-precipitation
 290 and four peaks for the sample prepared by impregnation. Some nickel oxide species are reduced at high
 291 temperatures (806-810 °C, peak 4), likely as a result of spinel formation. As for the samples prepared by
 292 impregnation, we still notice the reduction peak due to the formation of nickel oxide in weak interaction
 293 with the support (323 °C, peak 1). As for the Fe₂O₃ iron oxide species, the peak at 366, 400 or 430 °C
 294 (peak 2) is attributed to the reduction of Fe₂O₃ iron species into Fe₃O₄, while the peak at a higher
 295 temperature (625-650 °C, peak 3) is due to the reduction of Fe₃O₄ species to Fe⁰ [54] according to the
 296 equations (eq. S1) presented in the supplementary material sheet. The theoretical value (5.37×10^3
 297 $\mu\text{mol.g}^{-1}$) of hydrogen consumption is higher than those obtained experimentally. These results indicate
 298 that some of the species have not been completely reduced into metal. As it can be seen in table 3, the
 299 experimental H₂ consumption of the fourth peak in NiMgAlFe samples is higher of 37% when the
 300 ultrasound is used in the maturation phase compared to the traditional co-precipitation, and 30%
 301 compared to the impregnation method. These findings confirm that while using ultrasound, the nickel
 302 species is more accessible on the surface. Regarding the effect of iron on the reducibility of the nickel
 303 species, if the same preparation method is chosen, the H₂ consumption for the reduction of nickel oxide of
 304 NiMgAl US is $1.68 \times 10^3 \mu\text{mol.g}^{-1}$ while it is $0.43 \times 10^3 \mu\text{mol.g}^{-1}$ for NiMgAlFe US. This shows that a
 305 part of the nickel is covered by iron or that iron takes the place of nickel on the surface.

306

307 **Table 3.** Experimental and theoretical H₂ consumption for each peak of the calcined samples.

Sample	Experimental H ₂ consumption (10 ³ μmol.g ⁻¹)					Theoretical H ₂ consumption (10 ³ μmol.g ⁻¹)			
	Peak 1	Peak 2	Peak 3	Peak 4	Total	Peak 2	Peak 3	Peak 4+1	Total
NiMgAl Cp	-	-	-	1.33	1.33	-	-	1.7	1.7
NiMgAl Us	-	-	-	1.68	1.68	-	-	1.7	1.7
NiMgAl Imp	0.118	-	-	1.55	1.67	-	-	1.7	1.7
NiMgAlFe Cp	-	0.265	0.903	0.270	1.44	0.42	3.38	1.57	5.37
NiMgAlFe Us	-	0.125	1.385	0.43	1.94	0.42	3.38	1.57	5.37
NiMgAlFe Imp	0.019	0.035	0.245	0.299	0.62	0.42	3.38	1.57	5.37

308

309

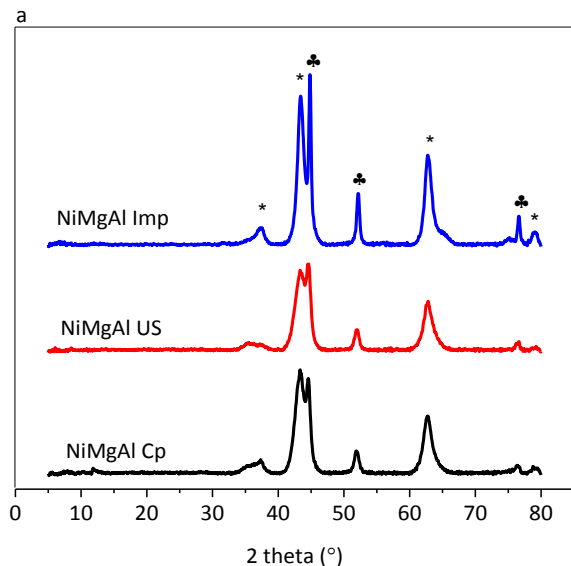
310

311 **3.3. Characterization of reduced samples**

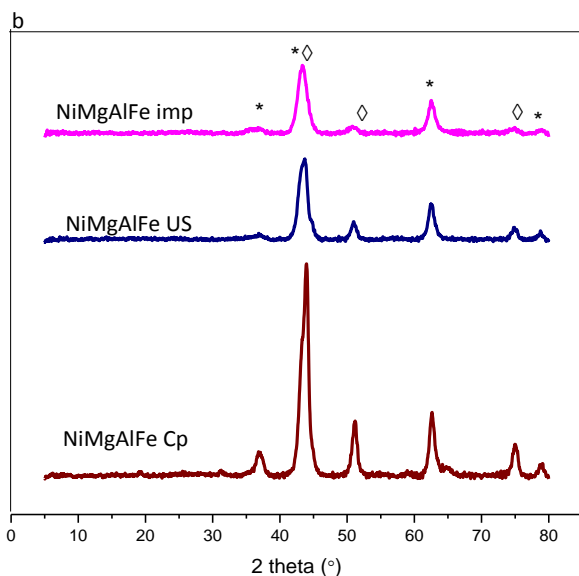
312

313 The calcined samples were reduced at 800 °C during 2 h under pure hydrogen flow. The X-ray
 314 diffractograms of all the reduced samples NiMgAl samples (figure 4 (a)) prepared by the three
 315 preparation methods were compatible with the following structures: MgO periclase, and metallic nickel.
 316 The X-ray diffractograms for the reduced NiMgAlFe samples (figure 4 (b)) show the presence of a new
 317 phase corresponding to Fe_{0.64}-Ni_{0.36}, and the absence of metallic nickel. This confirms that a large amount
 318 of iron can hinder the formation of metallic nickel (active phase for CO₂ methanation) [48].

319



320



321

322 **Figure 4.** X-ray diffraction patterns of the reduced samples (a), (b).

323 * MgO periclase JCPDS N° 43-1022, ♣ Ni nickel JCPDS N° 04-0850, ⬠ Fe_{0.64}-Ni_{0.36} iron nickel JCPDS
 324 N° 47-1405.

325

326 Figure 5 displays representative TEM-measured particle size distributions for the reduced NiMgAl series
 327 (the corresponding TEM images of the samples are shown in figure S4-S6 in the supplementary material
 328 sheet). In the case of the NiMgAl Cp catalyst (figure 5 (a)), a heterogeneous distribution of nickel
 329 particles is observed and their average diameter is 13.1 nm, while it is 8.2 nm for the NiMgAl US catalyst
 330 (figure 5 (b)), and 15.2 nm for NiMgAl Imp catalyst (figure 5 (c)). These results agree with the crystallite

331 size obtained from XRD (Table 4). This study reveals that the ultrasound assisted co-precipitation method
 332 allows decreasing the size of the particles. Similar results were obtained by Kim et al. [55] who confirm
 333 that the preparation methods influence the morphology and size of the metal particles. As an example, the
 334 scanning transmission electron microscopy (STEM) image of the NiMgAl Cp catalyst shows a good
 335 dispersion of heavy nanoparticles (bright spots) on the matrix (Figure 6). The scanning mode was used to
 336 get local and precise chemical analysis at the nanometer scale. However, the results of element mapping
 337 suggest a good dispersion of the elements (Mg, Al, O, and Ni) and a high homogeneity of them, based on
 338 an analysis of several zones, randomly selected. Figure 7 shows one of these zones. These results confirm
 339 the advantages of using LDH precursors in order to obtain homogeneous catalytic materials. They also
 340 confirm the identity of nickel particles as observed in Figure 6. To investigate the crystal structure of the
 341 Ni particles, high resolution TEM (HRTEM) was performed. Figure 8 shows a HRTEM image of an
 342 individual particle. Fast Fourier Transform (FFT) on this area reveals the characteristic pattern of the
 343 cubic phase for metallic nickel [56].

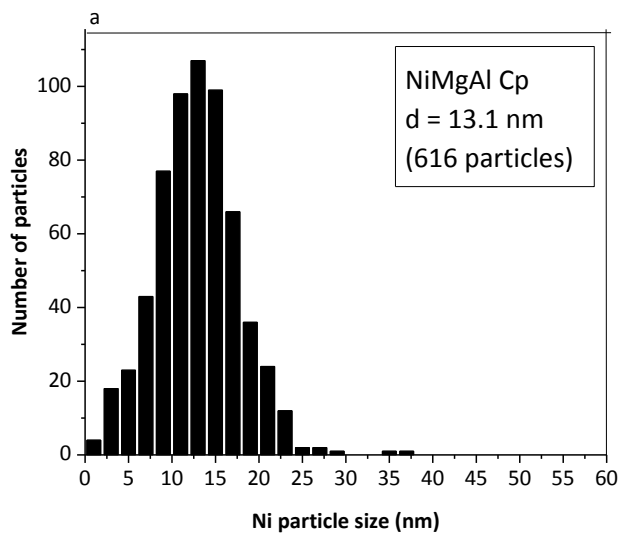
344

345 **Table 4.** Nickel particle and crystallite size and Ni-Fe crystallite size.

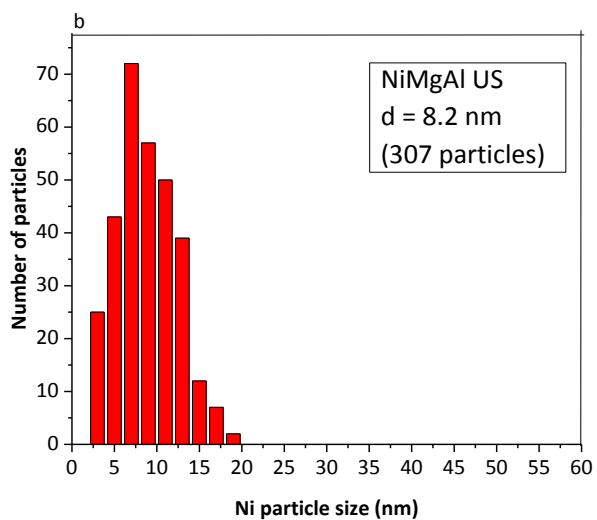
Catalyst	Ni crystallite size (nm) ^[a]	Ni particle size (nm) ^[b]	Ni-Fe crystallite size (nm) ^[a]
NiMgAl Cp	11.1	13.1	-
NiMgAl US	10.0	8.2	-
NiMgAl Imp	17.4	15.2	-
NiMgAlFe Cp	-	-	11.5
NiMgAlFe US	-	-	10.2
NiMgAlFe Imp	-	-	14.3

346 [a] Ni and Ni-Fe crystallite size determined by Debye-scherrer equation based on (200) peak.

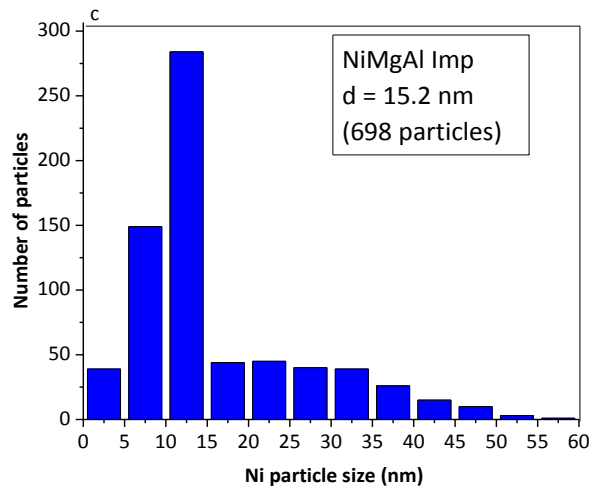
347 [b] Ni particle size determined by TEM analysis, Ni-Fe particle size not measured by TEM analysis



348

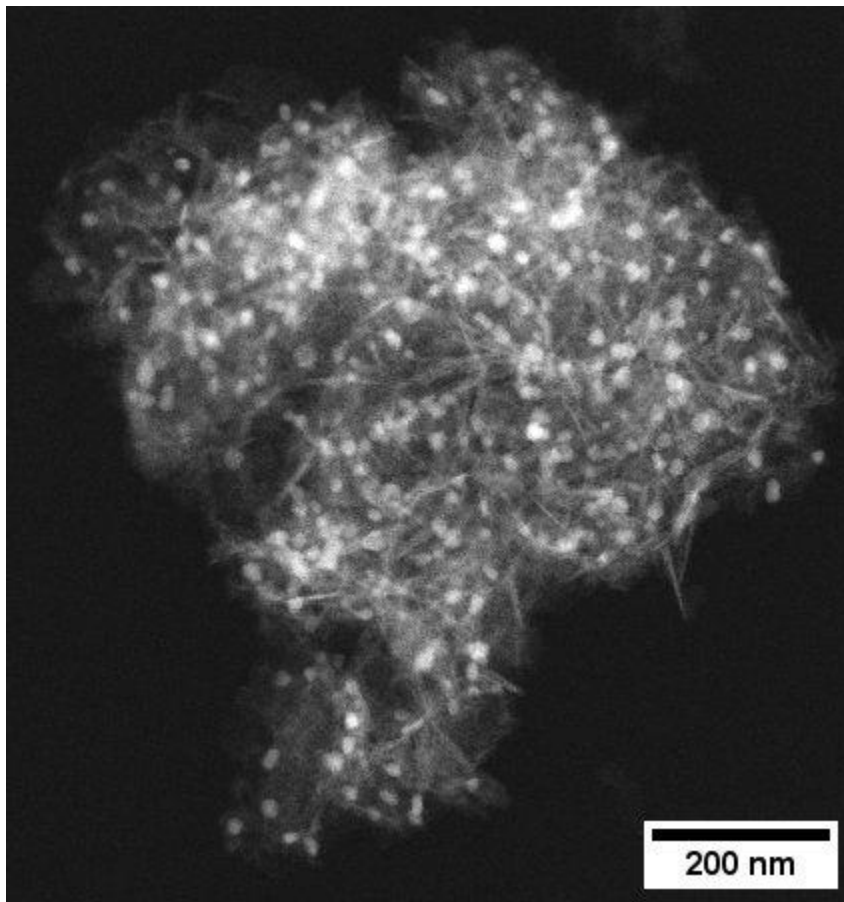


349



350

351 **Figure 5.** TEM-measured Ni Particle size distributions for the reduced (a) NiMgAl Cp , (b) NiMgAl US ,
352 and (c) NiMgAl Imp.

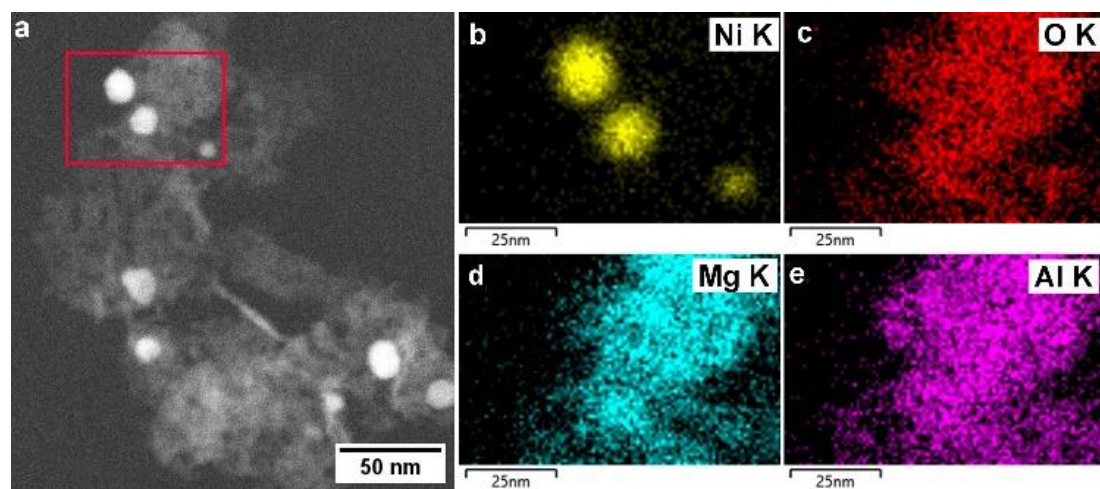


353

354

355 **Figure 6.** STEM-HAADF image of NiMgAl Cp.

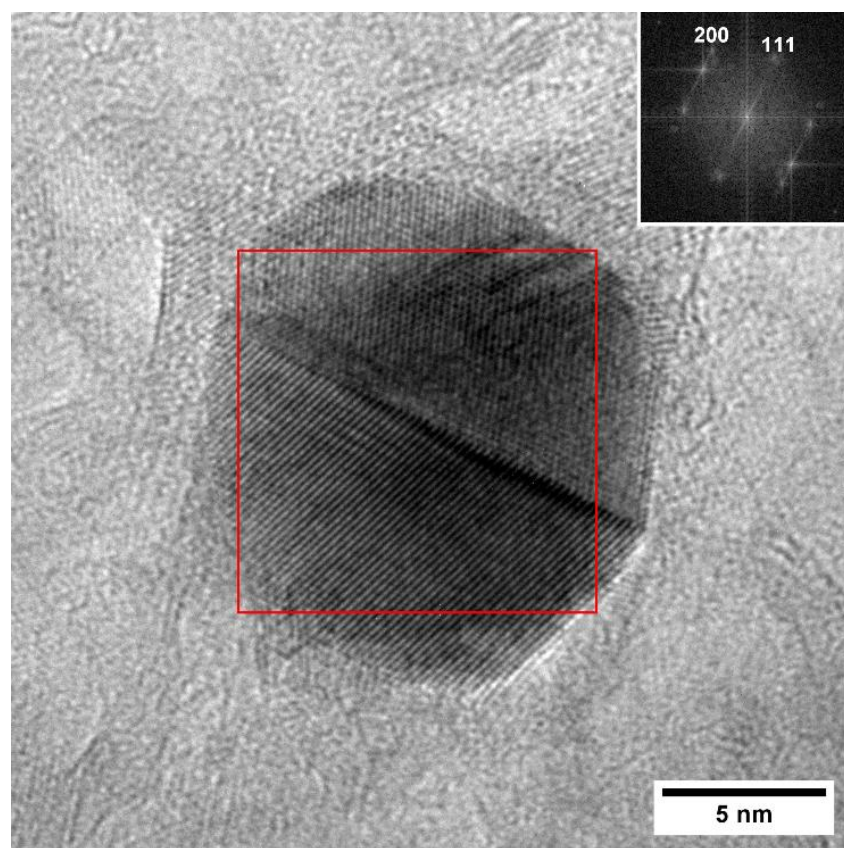
356



357

358 **Figure 7.** (a) STEM-HAADF image and corresponding (b-e) STEM-EDX maps.

359



360

361 **Figure 8.** HRTEM image of a nickel particle of the NiMgAl Cp sample. The inset shows the FFT of the
362 red squared area.

363

364 **3.4. Catalytic activity**

365

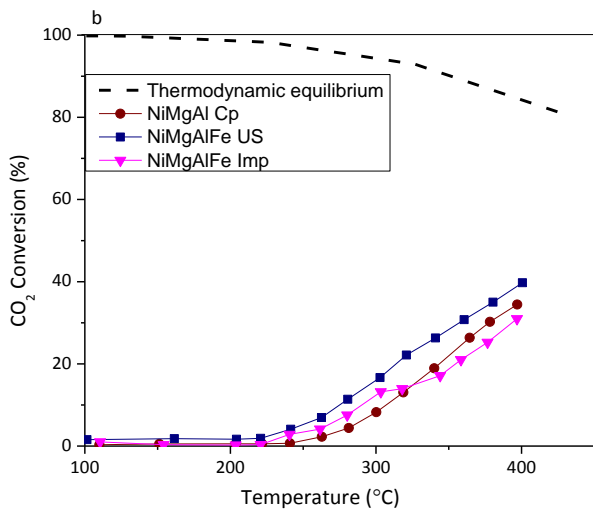
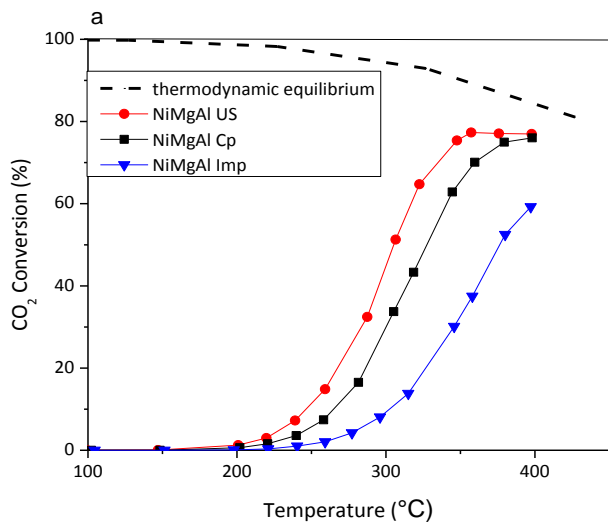
366 Figure 9 shows the catalytic performance in CO₂ conversion over NiMgAl and NiMgAlFe catalysts
367 prepared by co-precipitation, ultrasonic assisted co-precipitation and impregnation. Thermodynamics
368 state that practically total CO₂ conversion is achievable at lower temperatures, and that it declines with
369 rising temperature, as indicated by the dashed line (Figure 9.a, 9.b and 9.d), due to the coexistence of
370 parallel processes which produce undesirable side products, including carbon monoxide. All catalysts
371 show negligible CO₂ conversion at temperatures below 200 °C (Figure 9.a, 9.b and 9.d). The conversion
372 of CO₂ increases with temperature. Indeed, although the methanation reaction is exothermic, the
373 activation of the CO₂ molecule, which is very stable, requires a significant energy input due to its
374 chemical inertia. This energy is provided in thermal form. The conversion of CO₂ varies according to the
375 following order: NiMgAl US > NiMgAl Cp > NiMgAl Imp > NiMgAlFe US > NiMgAlFe Cp > NiMgAlFe
376 Imp. Moreover, all the catalysts of the NiMgAl series are very selective to methane, while the catalysts of
377 the NiMgAlFe series are more selective in CO than in CH₄ (Table 5). This can be related to the presence
378 of a high amount of iron. The NiMgAl US catalyst shows the best conversions amounting to
379 approximately 80% at 400 °C. The NiMgAl US catalyst is also very selective towards CH₄ production
380 with selectivity values close to 100% (Table 5). This can be related firstly to the higher specific surface
381 area and larger pore volume, secondly to the higher amount of reducible species as shown by H₂-TPR,
382 and thirdly to the smaller Ni particle size. Regarding the samples containing iron, whatever the
383 preparation method, their CO₂ conversion and selectivity to methane decrease as compared to samples
384 without iron. This may be due to the presence of a large amount of iron in the samples (mass content =
385 14%). This effect was demonstrated by Pandey et al. [57] who prepared a series of unsupported Ni-Fe
386 bimetallic catalysts. These authors showed that when going from a weight content of 10% Fe to 25%, the
387 CH₄ yield decreased from 80% to 30%. This result would be due to the decrease of the specific surface
388 area and pore volume when the iron content increases. This may also be due to the fact that a high amount
389 of iron promotes the reverse water gas shift reaction (RWGS), leading to high CO selectivity [36]. Fe₂O₃
390 phase is present in the sample NiMgAlFe as shown in XRD results. Therefore, according to TPR results,
391 the H₂ consumption for the reduction of nickel oxide of NiMgAl US is 1.86 x 10³ μmol.g⁻¹ while it is 0.43
392 x 10³ μmol.g⁻¹ for NiMgAlFe US. We can conclude that a part of the nickel is covered by iron or that iron
393 takes the place of nickel on the surface. In addition, when Fe₂O₃ is present in a catalyst, a different
394 mechanism can occur during the methanation reaction. The formate species is not stable and is
395 decomposed to CO by a reverse gas-to-water shift reaction [14,58–60]. Then, the carbon monoxide might
396 be converted to metal carbide and directly gives C1 to higher hydrocarbons (including olefins and
397 kerosenes) especially at high pressure [58,61]. On the other hand, Ni-based catalysts convert CO₂ to
398 carbonate and then to formate leading to the formation of methane [62]. The H₂-TPR and TEM analysis

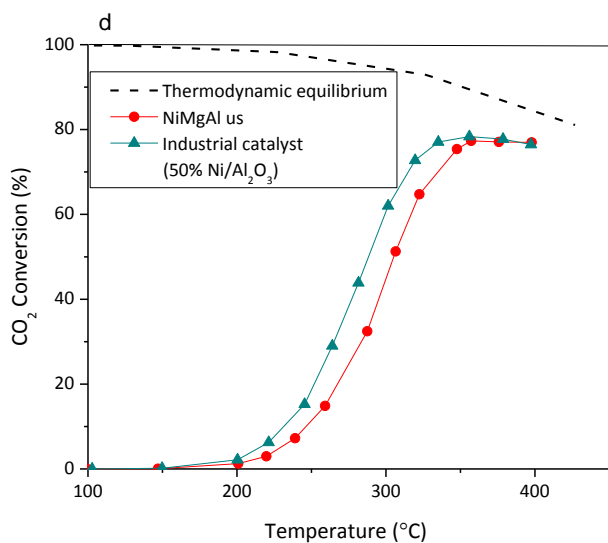
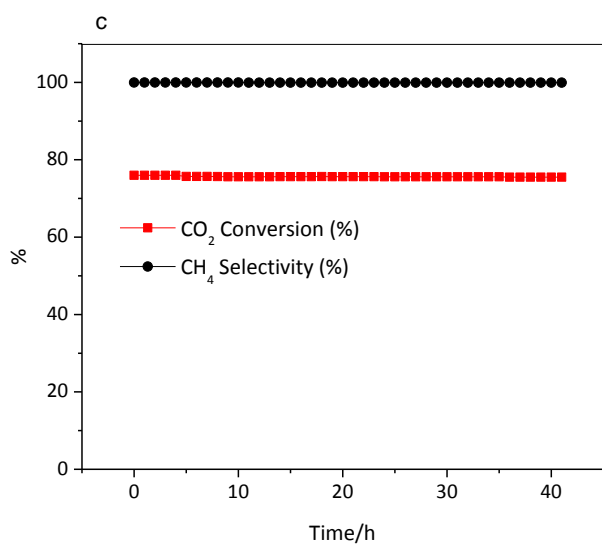
399 showed that in NiMgAl US catalyst, the nickel active phase is better dispersed. These results revealed that
400 using ultrasound during the maturation increases the distribution of the active phase. Figure 9.c shows the
401 stability test of NiMgAl US. The latter remains stable for 40 h under stream with no deactivation. A
402 comparison between our best catalyst NiMgAl US and industrial catalyst 50%Ni/Al₂O₃ is shown in Figure
403 9.d. At 400 °C, CO₂ conversion for both catalysts is approximately the same (80%), but the industrial
404 catalyst started to convert CO₂ at lower temperature. However, it is important to mention that our catalyst
405 contains only 10wt% of nickel while the industrial catalyst contains 50wt%. This makes our catalyst
406 significantly and advantageously cheaper than the industrial one. In addition, in order to verify the
407 presence of carbon and particle sintering, XRD and thermal analysis were carried out on the samples after
408 catalytic testing. The results of the thermal analysis showed only one exothermic peak attributed to the
409 oxidation of metallic nickel, and the results of the XRD analysis showed that the size of the nickel
410 crystals exhibited the same trend before and after the catalytic test. Thus, we can conclude that for all
411 three preparation methods and for the NiMgAl and NiMgAlFe samples, there is no presence of carbon or
412 particle sintering (results are presented in the supplementary material).

413 Data from studies that were published on CO₂ methanation in the presence of various catalysts are
414 summarized in Table S2 presented in supplementary material sheet. The catalyst reported in the present
415 study is more effective than most of the already reported catalysts, with a CO₂ conversion of
416 approximately 80% and a CH₄ selectivity of 99.9%. The catalyst 50%Ni/C catalyst prepared by
417 Gonçalves et al. was evaluated with a GHSV (60000 mL.g⁻¹.h⁻¹), different than that employed in this work
418 (40000 mL.g⁻¹.h⁻¹), and had a CO₂ conversion of 82% at 400 °C [63]. Consequently, a greater Ni
419 concentration is the cause of the substantially higher CO₂ conversion. On the other hand, the Ni(59%)
420 LDH catalyst prepared by Bette et al. converted 74% of the CO₂ at 350 °C [31] and the
421 15%Ni/Ce_{0.72}Zr_{0.28}O₂ catalyst prepared by Ocampo et al. [64] converted 82% of CO₂ at 400 °C under
422 different GHSV and higher amount of nickel. In addition, the 20%Ni-3%Fe/Al₂O₃-ZrO₂ catalyst
423 synthesized by Wu et al. converted 70% of the CO₂ at 400 °C [65] with a higher amount of nickel and a
424 small amount of iron. In addition, our catalyst is more effective than those made by Alcalde-Santiago et
425 al. [66], Wierzbicki et al. [67], Dias et al. [68], and Ashok et al. [69] utilizing LaOx, mixed oxides made
426 from LDH, SiO₂, and ZrO₂-CeO₂ as supports, although with the same nickel loading (10wt%).

427 This succinct summary was used to compare the NiMgAl US performance to studies that were published
428 in the literature [31,63–71]. Considering crucial factors like metal loading, and contact time, and price,
429 our NiMgAl US catalyst prepared by ultrasound-assisted co-precipitation method looks to be very active
430 in the CO₂ methanation reaction.

431





432

433 **Figure 9.** CO₂ conversion on (a) NiMgAl samples, and (b) NiMgAlFe samples (P = 1 atm, H₂/CO₂ = 4
 434 and GHSV = 6000 h⁻¹), (c) long-term stability test over NiMgAl US catalysts at 400 °C (H₂/CO₂=4, and
 435 GHSV=6000 h⁻¹), and (d) CH₄ yield of NiMgAl US and industrial catalyst (50%Ni/Al₂O₃).

436 **Table 5.** CH₄ and CO selectivity of all the catalysts at 400 °C.

Catalyst	CH ₄ selectivity (%)	CO selectivity (%)
NiMgAl Cp	99.9	0.1
NiMgAl US	99.9	0.1
NiMgAl Imp	99.6	0.4

NiMgAlFe Cp	40	60
NiMgAlFe US	32	68
NiMgAlFe Imp	49	51
Industrial catalyst (50%Ni/Al ₂ O ₃)	99.9	0.1

437

438

439 **4. Conclusion**

440 NiMgAl and NiMgAlFe catalysts have been synthesized by three different preparation methods, namely
441 co-precipitation, ultrasound-assisted co-precipitation, and impregnation. They have been characterized
442 and tested for CO₂ methanation. In all the catalysts, 10% of nickel was added either by substituting
443 partially the magnesium or by impregnation. In order to explore the potential of having a high quantity of
444 iron on the reducibility of the catalyst as well as on the catalytic activity, 14wt% of iron was substituted
445 for aluminum in order to obtain a molar ratio Al/Fe=1 in the NiMgAlFe series. Thus, we can conclude
446 that the addition of iron, regardless of the preparation method, decreases CO₂ conversion and methane
447 selectivity. This would be due to the decrease in specific surface area and pore volume following the
448 presence of a large amount of iron in the samples (mass content = 14%), and it could be that a big amount
449 of iron takes the place of active nickel so hindering its activity. In addition, when Fe₂O₃, the formate
450 species is not stable and is decomposed to CO by a reverse gas-to-water shift reaction. However, the
451 NiMgAl Us catalyst was very effective in the CO₂ methanation reaction with only 10 wt% of nickel. It
452 achieved approximately 80% of CO₂ conversion at 400 °C with a selectivity close to 100% towards
453 methane production. Furthermore, it demonstrated flawlessly steady performance up to 40 h of operation.
454 Among all the preparation methods used in this study, the ultrasound-assisted co-precipitation is the best
455 method of preparation. First, it saves a lot of time during the synthesis process since ultrasound reduces
456 the required time of maturation from 18 h (traditional co-precipitation) to 30 minutes. Second, it permits
457 to increase the specific surface area and pore volume, to decrease the Ni particle size, as well as to
458 improve its reducibility. These results confirm that the use of acoustic cavitation is a useful innovative
459 method for obtaining solids with improved catalytic characteristics. We anticipate that this preparation
460 method using specific devices for ultrasonic generation with the possibility of modifying parameters such
461 as power, frequency, time and mode and not using ultrasonic baths whose purpose is to clean the
462 glassware can be used to synthesize different oxides for different applications saving time and energy. It
463 is important to mention that our catalyst shows competitive activity compared to a representative

464 industrial catalyst and it is significantly cheaper than the latter. This suggests that our catalyst offers great
465 potential to be employed in the methanation process.

466 **5. Acknowledgements**

467 The authors would like to thank the Lebanese University and the University of Littoral Coast Opal for
468 their financial support. The TEM microscopes are facilities of the Chemistry and Materials Federation of
469 Paris-Centre (FCMat) and were funded by Sorbonne Université, CNRS and Région Ile de France which
470 are gratefully acknowledged.

471

472 **6. Declaration of competing interest**

473

474 The authors declare that they have no known competing financial interests or personal relationships that
475 could have appeared to influence the work reported in this paper.

476

477 **7. Data availability**

478

479 Data will be made available on request.

480

481 **8. Appendix A. Supplementary data**

482

483 Supplementary data to this article can be found online at

484 **9. References**

485

- 486 [1] N.Z. Muradov, T.N. Veziroğlu, “Green” path from fossil-based to hydrogen economy: An
487 overview of carbon-neutral technologies, *Int. J. Hydrogen Energy*. 33 (2008) 6804–6839.
488 <https://doi.org/10.1016/j.ijhydene.2008.08.054>.
- 489 [2] J. Nowotny, T. Bak, D. Chu, S. Fiechter, G.E. Murch, T.N. Veziroglu, Sustainable practices: Solar
490 hydrogen fuel and education program on sustainable energy systems, *Int. J. Hydrogen Energy*. 39
491 (2014) 4151–4157. <https://doi.org/10.1016/j.ijhydene.2013.12.114>.
- 492 [3] S. Abate, K. Barbera, E. Giglio, F. Deorsola, S. Bensaid, S. Perathoner, R. Pirone, G. Centi,
493 Synthesis, Characterization, and Activity Pattern of Ni-Al Hydrotalcite Catalysts in CO₂
494 Methanation, *Ind. Eng. Chem. Res.* 55 (2016) 8299–8308.
495 <https://doi.org/10.1021/acs.iecr.6b01581>.
- 496 [4] P. Marocco, E.A. Morosanu, E. Giglio, D. Ferrero, C. Mebrahtu, A. Lanzini, S. Abate, S. Bensaid,
497 S. Perathoner, M. Santarelli, R. Pirone, G. Centi, CO₂ methanation over Ni/Al hydrotalcite-
498 derived catalyst: Experimental characterization and kinetic study, *Fuel*. 225 (2018) 230–242.
499 <https://doi.org/10.1016/j.fuel.2018.03.137>.
- 500 [5] E. Giglio, A. Lanzini, M. Santarelli, P. Leone, Synthetic natural gas via integrated high-
501 temperature electrolysis and methanation : Part I — Energy performance, *J. Energy Storage*. 1
502 (2015) 22–37. <https://doi.org/10.1016/j.est.2015.04.002>.
- 503 [6] J. Maton, L. Zhao, J. Brouwer, Dynamic modeling of compressed gas energy storage to
504 complement renewable wind power intermittency, *Int. J. Hydrogen Energy*. 38 (2013) 7867–7880.
505 <https://doi.org/10.1016/j.ijhydene.2013.04.030>.
- 506 [7] A.L. Kustov, A.M. Frey, K.E. Larsen, T. Johannessen, J.K. Nørskov, C.H. Christensen, CO

- 507 methanation over supported bimetallic Ni-Fe catalysts: From computational studies towards
508 catalyst optimization, *Appl. Catal. A Gen.* 320 (2007) 98–104.
509 <https://doi.org/10.1016/j.apcata.2006.12.017>.
- 510 [8] S. Rönsch, J. Schneider, S. Matthischke, M. Schlüter, M. Götz, J. Lefebvre, P. Prabhakaran, S.
511 Bajohr, Review on methanation – From fundamentals to current projects, *Fuel*. 166 (2016) 276–
512 296. <https://doi.org/10.1016/j.fuel.2015.10.111>.
- 513 [9] B. Miao, S.S.K. Ma, X. Wang, H. Su, S.H. Chan, Catalysis mechanisms of CO₂ and CO
514 methanation, *Catal. Sci. Technol.* 6 (2016) 4048–4058. <https://doi.org/10.1039/c6cy00478d>.
- 515 [10] C. Vogt, M. Monai, G.J. Kramer, B.M. Weckhuysen, The renaissance of the Sabatier reaction and
516 its applications on Earth and in space, *Nat. Catal.* 2 (2019) 188–197.
517 <https://doi.org/10.1038/s41929-019-0244-4>.
- 518 [11] P. Frontera, A. Macario, M. Ferraro, P.L. Antonucci, Supported catalysts for CO₂ methanation: A
519 review, *Catalysts*. 7 (2017) 1–28. <https://doi.org/10.3390/catal7020059>.
- 520 [12] A.S. Al-fatesh, S.O. Kasim, A.A. Ibrahim, A.I. Osman, A.E. Abasaeed, H. Atia, U. Armbruster, L.
521 Frusteri, Y. Mohammed, A.H. Fakeeha, Greenhouse gases utilization via catalytic reforming with
522 Sc promoted Ni /, *Fuel*. 330 (2022) 125523. <https://doi.org/10.1016/j.fuel.2022.125523>.
- 523 [13] H.L. Huynh, Z. Yu, CO₂ Methanation on Hydrotalcite-Derived Catalysts and Structured Reactors:
524 A Review, *Energy Technol.* 8 (2020). <https://doi.org/10.1002/ente.201901475>.
- 525 [14] R.A. El-salamony, A.S. Al-fatesh, K. Acharya, A.A.M. Abahussain, A. Bagabas, N.S. Kumar,
526 A.A. Ibrahim, W.U. Khan, R. Kumar, Carbon Dioxide Valorization into Methane Using Samarium
527 Oxide-Supported Monometallic and Bimetallic Catalysts Radwa, *Catalysts*. 13 (2023) 113.
528 <https://doi.org/10.3390/catal13010113>.
- 529 [15] W. Li, H. Wang, X. Jiang, J. Zhu, Z. Liu, X. Guo, C. Song, A short review of recent advances in
530 CO₂ hydrogenation to hydrocarbons over heterogeneous catalysts, *RSC Adv.* 8 (2018) 7651–
531 7669. <https://doi.org/10.1039/c7ra13546g>.
- 532 [16] Y.R. Dias, O.W. Perez-Lopez, CO₂methanation over Ni-Al LDH-derived catalyst with variable
533 Ni/Al ratio, *J. CO₂ Util.* 68 (2023) 102381. <https://doi.org/10.1016/j.jcou.2022.102381>.
- 534 [17] X. Guo, D. Gao, H. He, A. Traitangwong, Promotion of CO₂ methanation at low temperature over
535 hydrotalcite-derived catalysts-effect of the tunable metal species and basicity, *Int. J. Hydrogen
536 Energy*. 9 (2020) 193. <https://doi.org/10.1016/j.ijhydene.2020.09.193>.
- 537 [18] H.M.S. Al-Aani, E. Iro, P. Chirra, I. Fechete, M. Badea, C. Negrilă, I. Popescu, M. Olea, I.C.
538 Marcu, Cu_xCeMgAlO mixed oxide catalysts derived from multicationic LDH precursors for
539 methane total oxidation, *Appl. Catal. A Gen.* 586 (2019) 4–12.
540 <https://doi.org/10.1016/j.apcata.2019.117215>.
- 541 [19] G. Mishra, B. Dash, S. Pandey, Layered double hydroxides : A brief review from fundamentals to
542 application as evolving biomaterials, *Appl. Clay Sci.* 153 (2018) 172–186.
543 <https://doi.org/10.1016/j.clay.2017.12.021>.
- 544 [20] X. Wang, Z. Yu, L. Ye, M. Zhang, J. Xiong, R. Zhang, X. Li, N. Ji, X. Lu, Layered Double
545 Hydroxide-Derived Bimetallic Ni–Cu Catalysts Prompted the Efficient Conversion of γ -
546 Valerolactone to 2-Methyltetrahydrofuran, *ChemCatChem*. 14 (2022).
547 <https://doi.org/10.1002/cctc.202101441>.
- 548 [21] U. Costantino, F. Marmottini, M. Nocchetti, R. Vivani, New Synthetic Routes to Hydrotalcite-
549 Like Compounds - Characterisation and Properties of the Obtained Materials, *Eur. J. Inorg. Chem.*
550 (1998). [https://doi.org/10.1002/\(SICI\)1099-0682\(199810\)1998:10<1439::AID-](https://doi.org/10.1002/(SICI)1099-0682(199810)1998:10<1439::AID-)

- 551 EJIC1439>3.0.CO;2-1.
- 552 [22] F. Prinetto, G. Ghiotti, P. Gra, D. Tichit, Synthesis and characterization of sol - gel Mg / Al and Ni
553 / Al layered double hydroxides and comparison with co-precipitated samples, Microporous
554 Mesoporous Mater. 39 (2000) 229–247. [https://doi.org/10.1016/s1387-1811\(00\)00197-9](https://doi.org/10.1016/s1387-1811(00)00197-9).
- 555 [23] U. Sikander, S. Sufian, M.A. Salam, A review of hydrotalcite based catalysts for hydrogen
556 production systems, Int. J. Hydrogen Energy. 42 (2017) 19851–19868.
557 <https://doi.org/10.1016/j.ijhydene.2017.06.089>.
- 558 [24] A. Pérez, J. Lamonier, J. Giraudon, R. Molina, S. Moreno, Catalytic activity of Co – Mg mixed
559 oxides in the VOC oxidation : Effects of ultrasonic assisted in the synthesis, Catal. Today. 176
560 (2011) 286–291. <https://doi.org/10.1016/j.cattod.2010.11.088>.
- 561 [25] M. Shari, M. Haghghi, M. Abdollahifar, Hydrogen production via reforming of biogas over
562 nanostructured Ni/Y catalyst : Effect of ultrasound irradiation and Ni-content on catalyst
563 properties and performance, Mater. Res. Bull. 60 (2014) 328–340.
564 <https://doi.org/10.1016/j.materresbull.2014.07.027>.
- 565 [26] S. Allahyari, M. Haghghi, A. Ebadi, S. Hosseinzadeh, Ultrasound assisted co-precipitation of
566 nanostructured CuO – ZnO – Al₂O₃ over HZSM-5 : Effect of precursor and irradiation power on
567 nanocatalyst properties and catalytic performance for direct syngas to DME, Ultrason. -
568 Sonochemistry. 21 (2014) 663–673. <https://doi.org/10.1016/j.ultsonch.2013.09.014>.
- 569 [27] Y. Vafaeian, M. Haghghi, S. Aghamohammadi, Ultrasound assisted dispersion of different
570 amount of Ni over ZSM-5 used as nanostructured catalyst for hydrogen production via CO₂
571 reforming of methane, Energy Convers. Manag. 76 (2013) 1093–1103.
572 <https://doi.org/10.1016/j.enconman.2013.08.010>.
- 573 [28] M. Dinari, S. Mallakpour, Ultrasound-assisted one-pot preparation of organo-modified nano-sized
574 layered double hydroxide and its nanocomposites with polyvinylpyrrolidone, J. Polym. Res. 21
575 (2014) 350. <https://doi.org/10.1007/s10965-013-0350-y>.
- 576 [29] S.R. Yahyavi, M. Haghghi, S. Shafiei, M. Abdollahifar, F. Rahmani, Ultrasound-assisted
577 synthesis and physicochemical characterization of Ni-Co/Al₂O₃-MgO nanocatalysts enhanced by
578 different amounts of MgO used for CH₄/CO₂ reforming, Energy Convers. Manag. 97 (2015) 273–
579 281. <https://doi.org/10.1016/j.enconman.2015.03.064>.
- 580 [30] L. Yosefi, M. Haghghi, S. Allahyari, S. Ashkriz, Effect of ultrasound irradiation and Ni-loading
581 on properties and performance of CeO₂-doped Ni/clinoptilolite nanocatalyst used in polluted air
582 treatment, Process Saf. Environ. Prot. 95 (2015) 26–37.
583 <https://doi.org/10.1016/j.psep.2015.02.006>.
- 584 [31] N. Bette, J. Thielemann, M. Schreiner, F. Mertens, Methanation of CO₂ over a (Mg , Al)Ox
585 Supported Nickel Catalyst Derived from a (Ni, Mg, Al) -Hydrotalcite-like Precursor,
586 Chemcatchem Commun. 8 (2016) 2903. <https://doi.org/10.1002/cctc.201600469>.
- 587 [32] D.P. Debecker, E.M. Gaigneaux, G. Busca, Exploring, tuning, and exploiting the basicity of
588 hydrotalcites for applications in heterogeneous catalysis, Chem. - A Eur. J. 15 (2009) 3920–3935.
589 <https://doi.org/10.1002/chem.200900060>.
- 590 [33] H. Liu, D. Wierzbicki, R. Debek, M. Motak, T. Grzybek, P. Da Costa, M.E. Gálvez, La-promoted
591 Ni-hydrotalcite-derived catalysts for dry reforming of methane at low temperatures, Fuel. 182
592 (2016) 8–16. <https://doi.org/10.1016/j.fuel.2016.05.073>.
- 593 [34] Y. Sun, J. Zhou, W. Cai, R. Zhao, J. Yuan, Hierarchically porous NiAl-LDH nanoparticles as
594 highly efficient adsorbent for p-nitrophenol from water, Appl. Surf. Sci. 349 (2015) 897–903.
595 <https://doi.org/10.1016/j.apsusc.2015.05.041>.

- 596 [35] F.B.D. Saiah, B.L. Su, N. Bettahar, Nickel-iron layered double hydroxide (LDH): Textural
597 properties upon hydrothermal treatments and application on dye sorption, *J. Hazard. Mater.* 165
598 (2009) 206–217. <https://doi.org/10.1016/j.jhazmat.2008.09.125>.
- 599 [36] D. Wierzbicki, M.V. Moreno, S. Ognier, M. Motak, T. Grzybek, P. Da Costa, M.E. Gálvez, Ni-Fe
600 layered double hydroxide derived catalysts for non-plasma and DBD plasma-assisted CO₂
601 methanation, *Int. J. Hydrogen Energy.* 45 (2020) 10423–10432.
602 <https://doi.org/10.1016/j.ijhydene.2019.06.095>.
- 603 [37] C. Tanios, S. Bsaibes, C. Gennequin, M. Labaki, F. Cazier, S. Billet, H.L. Tidahy, B. Nsouli, A.
604 Aboukaïs, E. Abi-Aad, Syngas production by the CO₂ reforming of CH₄ over Ni–Co–Mg–Al
605 catalysts obtained from hydrotalcite precursors, *Int. J. Hydrogen Energy.* 42 (2017) 12818–12828.
606 <https://doi.org/10.1016/j.ijhydene.2017.01.120>.
- 607 [38] D. Li, M. Koike, J. Chen, Y. Nakagawa, K. Tomishige, Preparation of Ni-Cu/Mg/Al catalysts
608 from hydrotalcite-like compounds for hydrogen production by steam reforming of biomass tar, *Int.*
609 *J. Hydrogen Energy.* 39 (2014) 10959–10970. <https://doi.org/10.1016/j.ijhydene.2014.05.062>.
- 610 [39] C. Rizescu, C. Sun, I. Popescu, A. Urdă, P. Da Costa, I.C. Marcu, Hydrodeoxygenation of benzyl
611 alcohol on transition-metal-containing mixed oxides catalysts derived from layered double
612 hydroxide precursors, *Catal. Today.* 366 (2021) 235–244.
613 <https://doi.org/10.1016/j.cattod.2020.04.055>.
- 614 [40] R. Mrad, R. Cousin, C. Poupin, A. Aboukaïs, S. Siffert, Propene oxidation and NO reduction over
615 MgCu-Al(Fe) mixed oxides derived from hydrotalcite-like compounds, *Catal. Today.* 257 (2015)
616 98–103. <https://doi.org/10.1016/j.cattod.2015.02.020>.
- 617 [41] O.R. Macedo, N.F.P. Ribeiro, C.A.C. Perez, M. Schmal, M.M.V.M. Souza, Incorporation of
618 cerium ions by sonication in Ni – Mg – Al layered double hydroxides, *Appl. Clay Sci.* 48 (2010)
619 542–546. <https://doi.org/10.1016/j.clay.2010.02.015>.
- 620 [42] M.J. Climent, A. Corma, S. Iborra, K. Epping, A. Veltý, Increasing the basicity and catalytic
621 activity of hydrotalcites by different synthesis procedures, *J. Catal.* 225 (2004) 316–326.
622 <https://doi.org/10.1016/j.jcat.2004.04.027>.
- 623 [43] R. Ambati, P.R. Gogate, Ultrasound assisted synthesis of iron doped TiO₂ catalyst, *Ultrason.*
624 *Sonochem.* 40 (2018) 91–100. <https://doi.org/10.1016/j.ultsonch.2017.07.002>.
- 625 [44] R. Prasad, S. V. Dalvi, Sonocrystallization: Monitoring and controlling crystallization using
626 ultrasound, *Chem. Eng. Sci.* 226 (2020) 115911. <https://doi.org/10.1016/j.ces.2020.115911>.
- 627 [45] K. Seo, S. Suzuki, T. Kinoshita, I. Hirasawa, Effect of Ultrasonic Irradiation on the Crystallization
628 of Sodium Acetate Trihydrate Utilized as Heat Storage Material, *Chem. Eng. Technol.* 35 (2012)
629 1013–1016. <https://doi.org/10.1002/ceat.201100680>.
- 630 [46] S. Naseem, B. Gevers, R. Boldt, F.J.W.J. Labuschagné, A. Leuteritz, Comparison of transition
631 metal (Fe, Co, Ni, Cu, and Zn) containing tri-metal layered double hydroxides (LDHs) prepared
632 by urea hydrolysis, *R. Soc. Chem. Adv.* 9 (2019) 3030–3040. <https://doi.org/10.1039/c8ra10165e>.
- 633 [47] D.C. Carvalho, N.A. Ferreira, J.M. Filho, O.P. Ferreira, J.M. Soares, A.C. Oliveira, Ni – Fe and
634 Co – Fe binary oxides derived from layered double hydroxides and their catalytic evaluation for
635 hydrogen production, *Catal. Today.* 250 (2015) 155–165.
636 <https://doi.org/10.1016/j.cattod.2014.08.010>.
- 637 [48] C. Mebrahtu, F. Krebs, S. Perathoner, S. Abate, G. Centi, R. Palkovits, Hydrotalcite based Ni – Fe
638 /(Mg, Al)Ox catalysts for improved CO dissociation, basicity, and particle size, *Catal. Sci.*
639 *Technol.* 8 (2018) 1016–1913. <https://doi.org/10.1039/C7CY02099F>.

- 640 [49] F. Rouquerol, J. Rouquerol, K.S.W. Sing, P. Lewellyn, G. Maurin, Adsorption by Powders and
641 Porous Solids: Principle, Methodology and Applications, Elsevier, 2013.
- 642 [50] T. Hosseini, M. Haghighi, H. Ajamein, Fuel cell-grade hydrogen production from methanol over
643 sonochemical coprecipitated copper based nanocatalyst: Influence of irradiation power and time
644 on catalytic properties and performance, *Energy Convers. Manag.* 126 (2016) 595–607.
645 <https://doi.org/10.1016/j.enconman.2016.07.056>.
- 646 [51] J. Kirchner, J.K. Anolleck, H. Lösch, S. Kureti, Methanation of CO₂ on iron based catalysts, *Appl.*
647 *Catal. B Environ.* 223 (2018) 47–59. <https://doi.org/10.1016/j.apcatb.2017.06.025>.
- 648 [52] R. Dębek, K. Zubek, M. Motak, M.E. Galvez, P. Da Costa, T. Grzybek, Ni-Al hydrotalcite-like
649 material as the catalyst precursors for the dry reforming of methane at low temperature, *Comptes*
650 *Rendus Chim.* 18 (2015) 1205–1210. <https://doi.org/10.1016/j.crci.2015.04.005>.
- 651 [53] H. Nguyen-Phu, T. Kim, Y. Kim, K.H. Kang, H. Cho, J. Kim, I. Ro, Role of phase in NiMgAl
652 mixed oxide catalysts for CO₂ dry methane reforming (DRM), *Catal. Today.* (2022).
653 <https://doi.org/10.1016/j.cattod.2022.08.036>.
- 654 [54] E. Amini, M. Rezaei, M. Sadeghinia, Low temperature CO oxidation over mesoporous CuFe₂O₄
655 nanopowders synthesized by a novel sol-gel method, *Cuihua Xuebao/Chinese J. Catal.* 34 (2013)
656 1762–1767. [https://doi.org/10.1016/s1872-2067\(12\)60653-6](https://doi.org/10.1016/s1872-2067(12)60653-6).
- 657 [55] J. Kim, D. Jin, T. Park, K. Kim, Effect of metal particle size on coking during CO₂ reforming of
658 CH₄ over Ni – alumina aerogel catalysts, *Appl. Catal. A Gen.* 197 (2000) 191–200.
659 [https://doi.org/10.1016/S0926-860X\(99\)00487-1](https://doi.org/10.1016/S0926-860X(99)00487-1).
- 660 [56] L. Lin, C.A. Gerlak, C. Liu, J. Llorca, S. Yao, N. Rui, F. Zhang, Z. Liu, S. Zhang, K. Deng, C.B.
661 Murray, J.A. Rodriguez, S.D. Senanayake, Effect of Ni particle size on the production of
662 renewable methane from CO₂ over Ni/CeO₂ catalyst, *J. Energy Chem.* 61 (2021) 602–611.
663 <https://doi.org/10.1016/j.jechem.2021.02.021>.
- 664 [57] D. Pandey, K. Ray, R. Bhardwaj, S. Bojja, K.V.R. Chary, G. Deo, Promotion of unsupported
665 nickel catalyst using iron for CO₂ methanation, *Int. J. Hydrogen Energy.* 43 (2018) 4987–5000.
666 <https://doi.org/10.1016/j.ijhydene.2018.01.144>.
- 667 [58] G. Kishan, M. Lee, S. Nam, M. Choi, K. Lee, The catalytic conversion of CO₂ to hydrocarbons
668 over Fe-K supported on Al₂O₃-MgO mixed oxides, *Catal. Letters.* 56 (1998) 215–219.
- 669 [59] F.A. De la Rosa-Priego, E.D. Gutierrez-López, T.A. Zepeda, M. Acosta-Alejandro, A.M. Venezia,
670 S. Fuentes-Moyado, B. Pawelec, J.N. Díaz-De-León, Enhanced CO₂ Hydrogenation to C₂+
671 Hydrocarbons over Mesoporous x%Fe₂O₃-Al₂O₃ Catalysts, *Ind. Eng. Chem. Res.* 60 (2021)
672 18660–18671. <https://doi.org/10.1021/acs.iecr.1c01453>.
- 673 [60] J. Weiß, Q. Yang, U. Bentrup, E. V Kondratenko, Operando DRIFT and In situ Raman
674 Spectroscopic Studies on Aspects of CO₂ Fischer-Tropsch Synthesis Catalyzed by Bulk Iron
675 Oxide-Based Catalysts, *ChemCatChem.* 14 (2022) 1–10. <https://doi.org/10.1002/cctc.202200577>.
- 676 [61] J. Kim, S. Lee, M. Kang, K. Lee, M. Choi, Y. Kang, Promotion of CO₂ Hydrogenation to
677 Hydrocarbons in Three-Phase Catalytic (Fe-Cu-K-Al) Slurry Reactors, *Korean J. Chem. Eng.* 20
678 (2003) 967–972. <https://doi.org/10.1007/BF02697307>.
- 679 [62] L. Deng, X. Liu, R. Wang, C. Wang, G. Zhou, Unsupported Ni-Co alloy as efficient catalysts for
680 CO₂ methanation, *J. Alloys Compd.* 918 (2022) 165472.
681 <https://doi.org/10.1016/j.jallcom.2022.165472>.
- 682 [63] L.P.L. Gonçalves, A. Serov, G. Mccool, M. Dicome, O.I. Lebedev, M.F.R. Pereira, Y. V Kolen,
683 New Opportunity for Carbon-Supported Ni-based Electrocatalysts : Gas-Phase CO₂ Methanation,

- 684 ChemCatChem. 13 (2021) 4770–4779. <https://doi.org/10.1002/cctc.202101284>.
- 685 [64] F. Ocampo, B. Louis, A.C. Roger, Methanation of carbon dioxide over nickel-based
686 Ce_{0.72}Zr_{0.28}O₂ mixed oxide catalysts prepared by sol-gel method, Appl. Catal. A Gen. 369
687 (2009) 90–96. <https://doi.org/10.1016/j.apcata.2009.09.005>.
- 688 [65] Y. Wu, J. Lin, Y. Xu, G. Ma, J. Wang, Transition Metals Modified Ni-M (M=Fe, Co, Cr and Mn)
689 Catalysts Supported on Al₂O₃-ZrO₂ for Low-Temperature CO₂ Methanation, ChemCatChem. 12
690 (2020) 3553–3559. <https://doi.org/10.1002/cctc.202000399>.
- 691 [66] V. Alcalde-Santiago, A. Davó-Quiñonero, D. Lozano-Castelló, A. Quindimil, U. De-La-Torre, B.
692 Pereda-Ayo, J.A. González-Marcos, J.R. González-Velasco, A. Bueno-López, Ni/LnOx Catalysts
693 (Ln=La, Ce or Pr) for CO₂ Methanation, ChemCatChem. 11 (2019) 810–819.
694 <https://doi.org/10.1002/cctc.201801585>.
- 695 [67] D. Wierzbicki, R. Baran, R. De, P. Da, M. Motak, T. Grzybek, M.E. G, The influence of nickel
696 content on the performance of hydrotalcite-derived catalysts in CO₂ methanation reaction, Int. J.
697 Hydrogen Energy. 42 (2017) 23548. <https://doi.org/10.1016/j.ijhydene.2017.02.148>.
- 698 [68] Y.R. Dias, O.W. Perez-Lopez, Carbon dioxide methanation over Ni-Cu/SiO₂ catalysts, Energy
699 Convers. Manag. 203 (2020) 112214. <https://doi.org/10.1016/j.enconman.2019.112214>.
- 700 [69] J. Ashok, M.L. Ang, S. Kawi, Enhanced activity of CO₂ methanation over Ni/CeO₂-ZrO₂
701 catalysts: Influence of preparation methods, Catal. Today. 281 (2017) 304–311.
702 <https://doi.org/10.1016/j.cattod.2016.07.020>.
- 703 [70] M.C. Bacariza, I. Graça, S.S. Bebiano, J.M. Lopes, C. Henriques, Micro- and mesoporous
704 supports for CO₂ methanation catalysts: A comparison between SBA-15, MCM-41 and USY
705 zeolite, Chem. Eng. Sci. 175 (2018) 72–83. <https://doi.org/10.1016/j.ces.2017.09.027>.
- 706 [71] Q. Liu, Y. Tian, One-pot synthesis of NiO/SBA-15 monolith catalyst with a three-dimensional
707 framework for CO₂ methanation, Int. J. Hydrogen Energy. 42 (2017) 12295–12300.
708 <https://doi.org/10.1016/j.ijhydene.2017.02.070>.

709

710

711

712

713

714

715

716

717